Analytical modeling of organic−inorganic $CH_3NH_3PbI_3$ perovskite resistive switching and its application for neuromorphic recognition

Yanyun Ren[1], Valerio Milo[2], Zhongqiang Wang[1*], Haiyang Xu[1*], Daniele Ielmini[2*], Jiangang Ma[1] and Yichun Liu[1]

[1]*Key Laboratory for UV Light-Emitting Materials and Technology (Northeast Normal University), Ministry of Education, 5268 Renmin Street, Changchun, China*

[2]*Dipartimento di Elettronica, Informazione e Bioingegneria, Italian Universities Nanoelectronics Team, Politecnico di Milano, 20133 Milan, Italy*

*E-mail:wangzq752@nenu.edu.cn; hyxu@nenu.edu.cn and daniele.ielmini@polimi.it

Abstract:

This paper presents an analytical model of resistive switching in organic−inorganic $CH_3NH_3PbI_3$ perovskite. The resistive switching phenomenon is interpreted as due to the formation/rupture of iodine vacancy based conductive filament propagating in both the vertical and the lateral direction. Set and reset processes are explained in the model by the evolution of the CF length and radius driven by electrical and thermal forces. The model-based simulation results can describe the experimental results, providing an estimate of several switching parameters such as the activation energy of iodine vacancy migration and the CF diameter. Learning in a 2-transistor/1-resistor synapse structure is demonstrated by simulations. Finally, the neuromorphic recognition of multiple patterns is demonstrated through a 2-layer neural network consisting of 5625 pre-synaptic neurons and 4 post-synaptic neurons.

I. Introduction

Resistive switching (RS) devices are attracting a broad interest for their potential applications in nonvolatile memories and neuromorphic computing circuits due to several advantages, such as low power consumption, high switching speed, high density and the capability to emulate the behavior of biological synapses [1]. So far, various materials have been reported to present RS processes, including metal-oxides [2], chalcogenides [3], inorganic perovskite [4], [5] and organic materials [6]. The hybrid organic−inorganic perovskite is well known as multi-functional material for applications in solar cells [7], light-emitting field-effect transistor [8], water photolysis [9]. In particular, the low-temperature operation of $CH_3NH_3PbI_3$ enables the development of flexible memory circuits, while its photovoltaic properties allow for applications for photo-read synaptic functions [4]. Also, Choi et al. reported Ag/CH_3NH_3PbI3/Pt device can evidence an ultralow electric field and high ON/OFF ratio switching behavior for multilevel data storage [10]. The RS mechanism was generally attributed to the migration of iodine vacancy (V_I) or bulk defects driven by electric-field [5], [11], however, although the numerical modeling is an irreplaceable method to investigate the RS dynamics [12]–[14], a comprehensive understanding of this mechanism is not so far achieved also for lack of dedicated compact analytical models for organic-inorganic perovskite materials.

Nowadays, neuromorphic computation, which aims at outperforming performances of Von Neumann architectures, is one of the most investigated topics in

artificial intelligence and neural network research. The hardware platform including RS devices has been regarded as promising candidate to build neuromorphic systems with low energy consumption and high density level [15]–[17]. Several structures (e.g., crossbar, artificial synapse schemes) based on resistive-RAM (RRAM) devices have been designed and used for pattern learning, face classification, sparse coding, both multiplier and other neuromorphic systems [16], [18]–[21] with great results. Furthermore, the development of an analytical model capable of capturing RS is crucial to build a theoretical basis allowing to implement neuromorphic computing with RRAM devices.

This work presents a physics-based analytical model to simulate the RS behavior in organic−inorganic perovskite via the growth and dissolution of a V_I-based conductive filament (CF), which is compared to experimental data. Particularly, a fundamental characteristic, such as activation energy of V_I migration process, is extracted by analyzing the dependence of retention time on temperature. Also, to demonstrate neuromorphic learning and recognition via organic−inorganic perovskite devices, a 2-transistor/1-resistor structure is designed as electronic synapse and enables to capture anti-STDP function, which is a well-known synaptic plasticity mechanism responsible for update of synaptic weights. Finally, multi-pattern learning and recognition are demonstrated via a 2-layer feed-forward neural network.

II. Resistive Switching Characterization

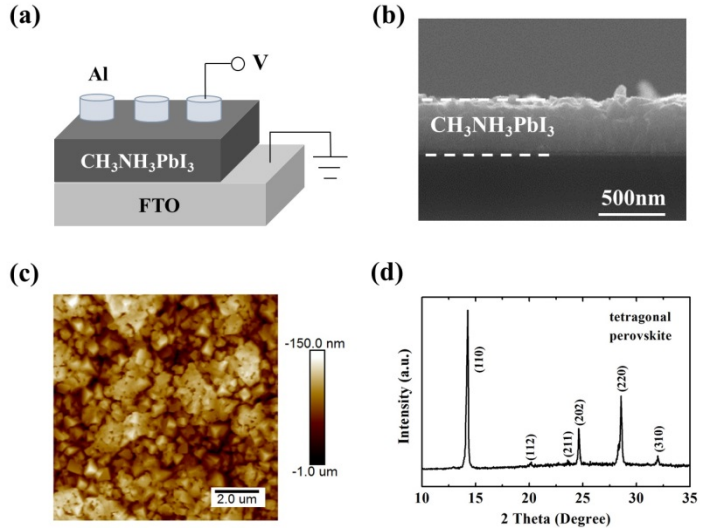

Figure 1. (a) Illustrative representation of the Al/$CH_3NH_3PbI_3$/FTO device whose structure is further described in detail by (b) a cross-sectional SEM image and (c) AFM image of the perovskite layer. (d) Typical XRD data of $CH_3NH_3PbI_3$ thin films. Diffraction peaks at 2θ equal to 14.2°, 28.6°, and 32.0° represent the crystal faces (110), (220), and (310) of tetragonal perovskite structure.

Figure 1(a) shows the structure of the perovskite device studied in this work, where a $CH_3NH_3PbI_3$ layer is sandwiched between an Al-based top electrode (TE) and a FTO-based bottom electrode (BE). A detailed vision of device structure is also provided by a cross-sectional SEM image (Figure 1(b)), which shows that the perovskite film has a uniform thickness of about 500 nm. In addition, the surface morphology of perovskite film has been characterized by atomic force microscopy (AFM) and the result, shown in Figure 1(c), evidences the high quality of perovskite film used in our experiments. Figure 1(d) also shows the result of an X-ray diffraction (XRD) experiment performed on our device showing the intensity diffraction peaks of tetragonal perovskite associated to angles 14.2°, 28.6°, and 32.0°, respectively, which in turn correspond to the crystal faces (110), (220), and (310).

To characterize the electrical properties of our perovskite device, a triangular voltage sweep, where positive/negative voltage causes reset/set transition, respectively, is applied to TE with BE grounded. Before activating cycling operation, a forming process under a high negative TE voltage is necessary to initialize the device. With increasing the voltage sweep, the current sharply increases up to reach the compliance current of 10 mA at $V_{Forming} = -1.2\ V$ inducing the formation of a CF in perovskite film. After forming, as shown in Figure 2(a), 100 reset/set cycles are performed to test the RS characteristics evidencing a reliable behavior with limited fluctuations. During reset phase, the current abruptly decreases at voltage $V_{reset} = 1.2\ V$ indicating a fast CF disruption. In contrast, a relatively slow current increase can be observed during set since the CF formation occur via a gradual process. Figure 2(b) and (c) shows the conductive-AFM images of both HRS and LRS to investigate the local conductivity distribution of our devices. The scanning area is $450 \times 450\ nm^2$ and the read voltage is 15 mV. Compared to the very low conductivity distribution corresponding to the high-resistance state (HRS), a high conductive path appears as the device reaches the low-resistance state (LRS), thus supporting the formation/rupture of CF as RS mechanism for our perovskite device. According to a previous work [5], the CF is most possibly composed of V_I driven by high electric field. However, a strong limit to achieve a complete understanding of RS dynamics is currently the lack of analytical models capable of capturing the RS behavior of perovskite devices.

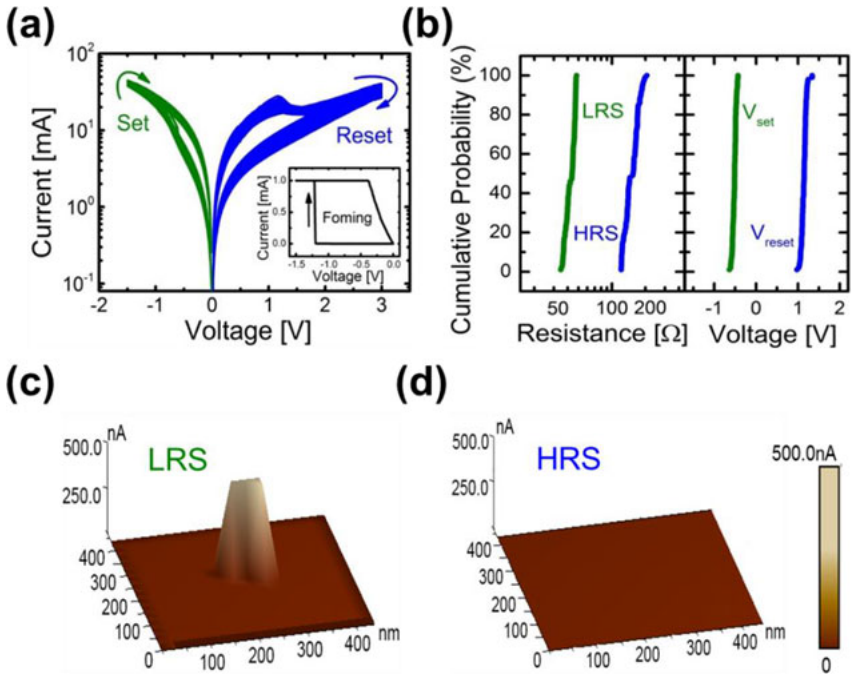

Figure 2. a) Measured I–V characteristics and b) the distribution of HRS/LRS and switching voltages for the Al/$CH_3NH_3PbI_3$/FTO-based perovskite device obtained after the forming process described in the top inset by 100 reset/set switching cycles under the application of triangular voltage sweeps. The conductive-AFM images show the local conductivity distribution of perovskite film in c) LRS and d) HRS, respectively.

III. Analytical Modeling

Based on the experimental results shown in Figure 2, we proposed a V_I migration-based analytical model to provide a comprehensive explanation of the RS characteristics in perovskite devices. As illustrated in Figure 3(a), our model mainly includes three operation phases: forming, reset and set transitions. During the forming process, a negative voltage applied to the TE induces a high electric field leading to the V_I nucleation followed by CF formation in the perovskite film, which enables to activate the RS operation for following cycles. The CF can be simplified as one cylinder, with radius r and height h, since there is an obvious boundary between CF (LRS) and outer region (HRS) as observed in Figure 2 (b) and (c). After forming, the application of a positive bias to the TE is at the origin of the V_I migration from TE to

BE resulting in the formation of a depleted region near TE, referred to as gap, and thus in a reset transition. Subsequently, a set transition induced by a negative bias at the TE allows to form the CF again, thus supporting RS cycling operation. Note that the application of a negative voltage drives the V_I migration in opposite direction, namely from BE to TE, which leads to the growth of a sub-filament with an increased radius that re-fills the gap region. The details of reset and set processes will be discussed in the following two sections.

Reset Transition

In correspondence of reset transition, V_I migration from TE to BE is activated by two fundamental processes, namely the Fick diffusion in combination with V_I drift. Fick diffusion is regulated by the equation $J_{Fick} = D\nabla n$, where $D = 0.5a^2 f exp(-E_a/kT)$ is the diffusivity coefficient and ∇n is V_I concentration gradient. In addition, regarding the coefficient *D*, a is vacancy hopping distance, f is escape-attempt frequency, E_a is activation energy for migration, k is Boltzmann constant and T is local temperature. Thus, *D* and ∇n are the two key parameters to describe diffusion process. Here, we assume that the V_I concentration gradient (∇n) complies with the distance-based exponential relations, namely, $dn/dy = \alpha_1 exp\left(-\beta_1/0.5(L-g)\right)$ and $dn/dx = \alpha_2 exp(-\beta_2/0.5(r-r_0))$ in the vertical and lateral directions, respectively, where L is the thickness of perovskite film, g is the gap length, r_0 is a constant and the four coefficients α_1, α_2, β_1 and β_2 are fitting parameters. Since the BE serves as V_I reservoir and the gradient direction is always from BE to TE, the Fick diffusion is expected to hinder the reset process.

Another critical factor for V_I migration is the voltage field-activated V_I drift, which can be expressed by equation $J_{drift} = -vn$, where $v = afexp(-E_a/kT)sinh(qaE/2kT)$ is the drift velocity, E is the electric field inside the CF and q is elementary charge.

Combining J_{Fick} and J_{drift} equations, the time evolution of gap length g can be expressed as follows:

$$\frac{dg}{dt} = D\alpha_1 e^{-\frac{\beta_1}{0.5(L-g)}} - v \quad . \tag{1}$$

It should be also noted that the Joule heating is transferred both along CF in vertical direction according to steady-state Fourier equation and from inner CF to outer region in lateral direction according to the Newton's law of cooling. In particular, an effective thermal conductance (k'_{th}) is used to model the thermal conduction ability between the inner and outer region. As the area of outer region is much larger, it has an effective thermal contact at room temperature (T_0). Therefore, the outer region temperature (T_{out}) is directly set to the room temperature, namely $T_{out} = T_0$. The local temperature along the CF direction T(z) can be expressed as follows:

$$k_{th} r \frac{dT^2}{dz^2} = -\mathrm{r}\frac{E^2}{\rho} - 2k'_{th}(T - T_{out}) \quad , \tag{2}$$

where k_{th} is the thermal conductivity and ρ is the electrical resistivity. As the depleted gap originates, the local temperature of fragmented CF is extracted by solving a piecewise defined function assuming the thermal conductivity and electrical resistivity k_{CF} and ρ_{CF} are set to be constants in the CF region. In contrast, the gap region is featured by k_{gap} and ρ_{gap} parameters with different physical characteristics. Specifically, k_{gap} shows a close relationship with the degree of

depletion dictated by g. Therefore, a g-based exponential law is developed to express the variable k_{gap}:

$$k_{gap} = k_{CF} + 1 - (1 + k_{CF} - k_0)^{\frac{g}{0.5L}} \quad , \tag{3}$$

where k_0 is the bulk perovskite thermal conductivity. The critical gap length $0.5\,L$ is defined as the length where the gap thermal conductivity reaches the value of bulk perovskite. Based on Poole-Frenkel conduction, gap resistivity is a function of electric field, namely $\rho_{gap} \propto exp(-Ea/2kT)$. By taking the first order expansion, this equation can be simplified as

$$\rho_{gap} = \frac{\rho_0}{1+\gamma E} \quad , \tag{4}$$

where γ is a constant and ρ_0 is the zero-field gap resistivity. Thus, as indicated in Figure 3(a), an arbitrary gap region appeared near TE because of the reset transition.

Set Transition

Set transition starts from the HRS achieved via reset process (Figure 3(a)). The application of a negative voltage induces V_I migration from BE to TE, which leads the gap region to be re-filled. A model of set kinetics based on Fick and Soret diffusion is proposed to simulate the re-filling process, where the growth of the sub-CF involves increase of the CF radius with time. Similar to reset transition, Fick diffusion is described by a V_I migration driven by the concentration gradient that coarsens the sub-CF. Based on Soret diffusion, V_I tends also to move toward the hotter region along the temperature gradient, as observed both in liquid and solid materials. Compared to Fick diffusion, Soret diffusion suppresses the growth of CF. Soret diffusion flux can be

expressed as $J_{Soret} = DS_{Soret}\nabla T$, where $S_{Soret} = -E_a/kT^2$ is the Soret diffusion coefficient. Like the concentration gradient, the temperature gradient (∇T) in lateral direction is given by $dT/dx = \alpha_3 exp(-\beta_3/(r - r_0))$, where α_3 and β_3 are fitting parameters. Combining J_{Fick} and J_{Soret} in set transition, the time evolution of CF radius is expressed as follows:

$$\frac{dr}{dt} = D * \left(\alpha_2 e^{-\frac{\beta_2}{r-r_0}} + S_{Soret}\alpha_3 e^{-\frac{\beta_3}{r-r_0}}\right) \quad (5)$$

Simulation Results

Figure 3(b) and (c) shows the simulation results obtained by our analytical model of perovskite devices including an experimental I-V curve with corresponding calculation and the evolution of T, g, r as a function of time. After forming process, the device is in the LRS, where $g = 0$. By applying a positive voltage with rate $\beta \approx 0.9\ Vs^{-1}$, the temperature and the electric field of CF increase until the voltage across the device reaches $V_{reset} = 1.2V$. At V_{reset}, the applied voltage mainly drops across the gap region and the gap growth rate reaches $135\ \mathrm{nms}^{-1}$ inducing an abrupt increase of resistance with a corresponding decrease of current. However, despite the increase of applied voltage, the electric field within the CF starts gradually decreasing during depletion process, thus slowing down the gap formation process. This argument allows to understand why the increase of gap length mainly occurs in the forward part of positive voltage sweep. In contrast, the application of a negative voltage induces a set transition from the final state achieved by reset transition. During set transition, V_I

migration from BE to TE causes the formation of a sub-CF in gap region with a gradual increase of CF radius. The continuous resistance decrease leads to a current increase inducing a higher Joule heating, which in turn accelerates the growth of sub-CF and accordingly decreases the device resistance. Therefore, the set transition is based on a positive feedback effect, as also demonstrated in HfO_2-based RRAM devices [22].

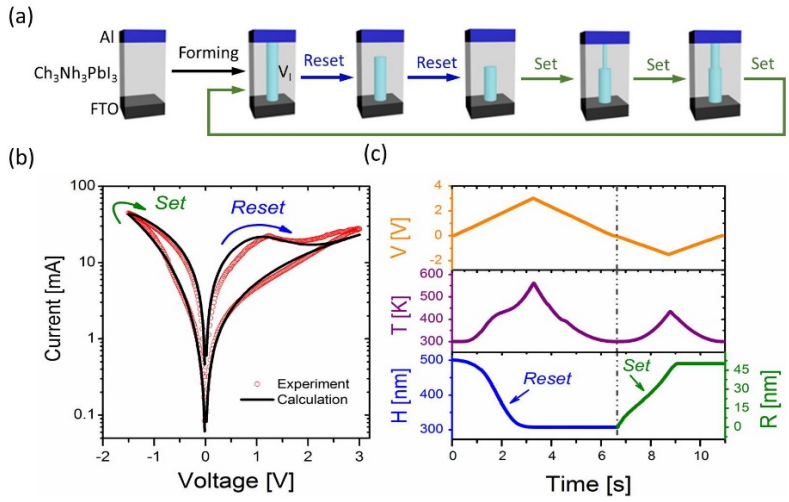

Figure 3. (a) Schematic illustration of RS modeling in Al/CH_3NH_3PbI3/FTO RRAM device, including CF evolution during forming, reset and set processes. (b) Measured and calculated I-V characteristics of the perovskite memory device evidencing set and reset transitions for negative and positive voltages, respectively. (c) Time evolution of calculated applied voltage waveform (top), temperature profile (center) and CF height and radius during reset/set operation cycle.

The combined effect of electrical and thermal driving forces, which can be both classified as voltage-based external factors, is at the origin of the evolution of CF in the RS mechanism. In addition, the self-characteristic of V_I migration is also dictated by the specific properties of $CH_3NH_3PbI_3$ material. In general, the activation energy for migration represents the barrier of V_I hopping from one position to another. As reported in literature [5], the retention time is a function of activation energy E_A according to the equation:

$$t_{reset} = t_0 e^{\frac{E_A}{kT}} \quad , \tag{6}$$

where t_0 is a pre-exponential factor. First, to calculate E_A, a constant voltage 1 mV is applied to device. As a result, E_A, which is a constant, and the local temperature T, obtained by solving Equation (2), depend only on T_0, which is varied from 200K to 320K.

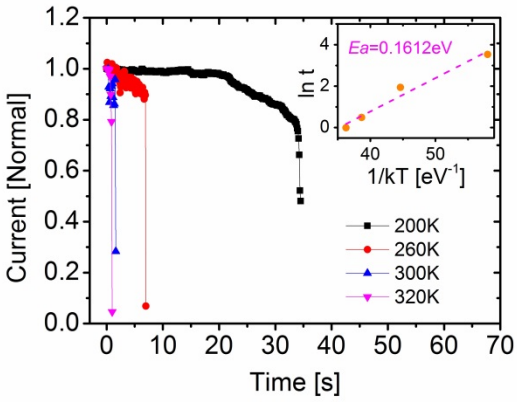

Figure 4. Representation of LRS retention behavior. The application of a constant read bias of amplitude 1 mV is to the similar initial state device enables to extract the retention times at room temperatures 200K, 260K, 300K, and 320K. The right inset shows the linear fitting between $t_{retention}$ expressed in log-scale and $1/kT$, which is calculated to obtain the activation energy of V_I.

Then, to extract the retention time for variable T_0, a linear fitting curve can be estimated between $ln(t_{retention})$ and $1/kT$. The slope of calculated fitting curve evidences E_A = 0.16 eV in accordance with typical values between 0.1 and 0.6 eV obtained in previous works [23]–[25], which are lower than the characteristic value for oxide-based devices (2.5eV). In particular, it should be noted that a lower activation energy makes the growth and rupture of CF much easier, thus supporting the potential application of perovskite-based RRAM devices for low power applications.

IV Neuromorphic learning and recognition

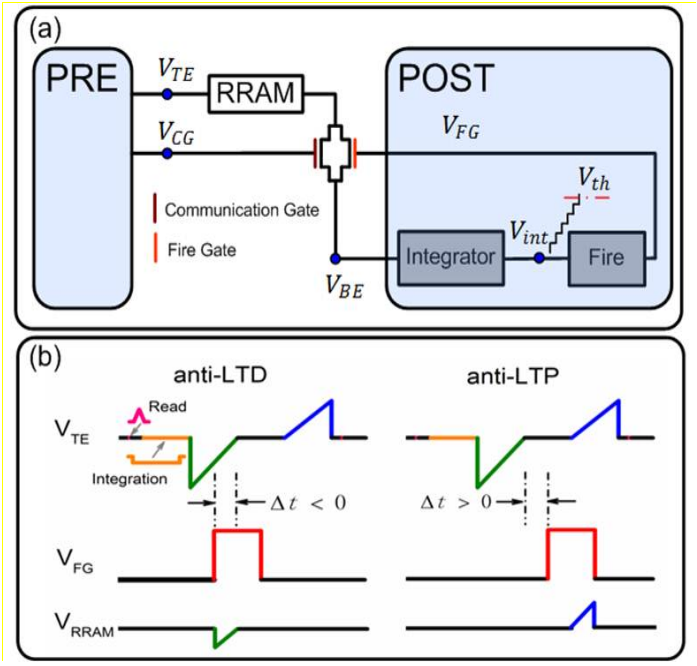

Figure 5. (a) Circuit scheme of a 2-transistor/1-resistor synapse structure. The PRE circuit drives the TE of RRAM device and the CG while the POST integrated the weighted current spikes coming from BE and controls the FG terminal sending a feedback fire spike as V_{int} reaches V_{th}. (b) Illustration of waveforms of voltages involved in 2T-1R synapse operation. If delay time between V_{TE} and V_{FG} is negative (left), a negative voltage due to signal overlap drops across RRAM causing a set transition, and thus anti-LTD process. Otherwise, if time delay is positive (right), the application of a positive voltage as a result of V_{TE} and V_{FG} overlap induces a reset transition, namely anti-LTP process.

The development of compact analytical models capable of capturing RS behavior of perovskite-based RRAM is crucial to explore novel applications requiring very complex structures including RRAM devices. To this purpose, we used our analytical model to simulate a 2-layer neuromorphic network designed for demonstrating learning and recognition of visual patterns via hybrid CMOS/RRAM synapses.

Figure 5(a) shows two circuital blocks implementing a pre-synaptic (PRE) and a post-synaptic (POST) neuron, respectively, communicating via a perovskite-based

electronic synapse with a 2-transistor/one-resistor (2T1R) structure. The PRE controls both the TE of RRAM device and the communication gate (CG) terminal applying the voltages V_{TE} and V_{CG}, respectively, while the POST drives the BE, which acts as the input of integrate circuit, and the fire gate (FG) terminal of synapse by a feedback voltage spike V_{FG}. The waveforms of V_{TE} and V_{FG} are illustrated in Figure 5(b). The top-electrode voltage V_{TE} consists of the sequence of 3 pulses with a duration of 100 ms, namely a negative triangular pulse of amplitude -2V followed by a period at zero voltage, which is in turn followed by a positive triangular pulse of amplitude 2V, while V_{CG} consists only of a 100-ms-long squared pulse of amplitude 8 V. The V_{TE} also includes two read pulses before and after the PRE and POST spikes to monitor the initial resistance R_0 and the final resistance R of RRAM. Their width and amplitude are set to 1 ms and 1 mV, respectively, to avoid any possible switching event.

During the communication phase, V_{TE} and V_{CG} are sent to the synapse at the same time inducing because of their time overlap a positive current flow toward the POST via BE. As a result, the integrator module in POST collects and integrates each PRE spike causing a gradual increase of internal potential V_{int}. As the latter reaches the neuron threshold V_{th} implemented by a comparator, the fire circuit within the POST sends a 100-ms-long square voltage pulse of amplitude 8 V to the FG terminal of 2T1R synapse.

As shown in Figure 5(b), if the time delay Δt between V_{TE} and V_{FG} spikes, which is defined as the time interval between the end of negative pulse within V_{TE} and the onset of V_{FG}, is negative ($\Delta t < 0$), the positive V_{FG} pulse overlaps with negative pulse

of V_{TE} spike by causing a negative voltage drop across the RRAM device resulting in a set transition (resistance decrease) via CF connection and thus in a long-term potentiation of the 2T1R synapse. In particular, as the synaptic potentiation is achieved for negative Δt values, such synaptic process is called anti-LTD, thus highlighting the opposite behavior compared to the typical biological STDP characteristics [26].

Otherwise, if the time delay is positive ($\Delta t > 0$), the overlap between V_{TE} and V_{FG} results in a positive voltage across RRAM inducing a reset transition via CF disconnection corresponding to a long-term depression (anti-LTP) of the 2T1R synapse.

It should be noted that the particular anti-STDP characteristics was also observed in some biological systems [27], which points out that the shape of STDP curves is not crucial to achieve high performance in neuromorphic tasks [28].

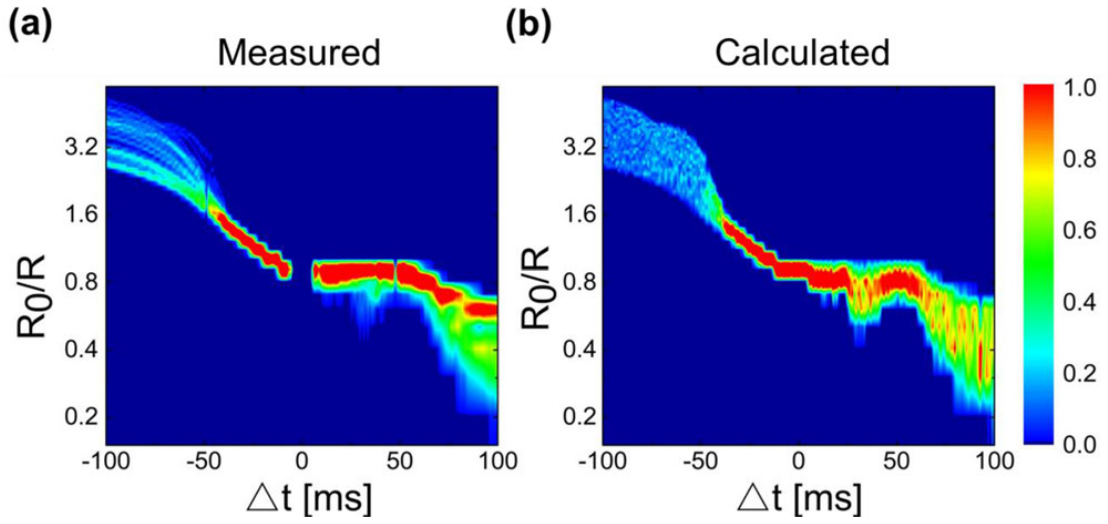

Figure 6. a) Measured and b) calculated ratio R_0/R as a function of time delay between PRE and POST spikes Δt for the perovskite-based RRAM evidencing anti-LTD gradual transitions for $\Delta t < 0$ and anti-LTP transitions for $\Delta t > 0$ with an abrupt resistance variation occurring for $\Delta t = 25$ ms. Experimental data show a high variability which is also observed in calculated results.

To validate the device capability to implement the anti-STDP, we calculated the ratio of initial and final resistances R_0/R for variable Δt.

Figure 6(a) shows the measured anti-STDP characteristics evidencing a gradual anti-LTD process for $\Delta t < 0$, which is due to nature of set transition in perovskite-based RRAM, and an abrupt anti-LTP process for $\Delta t > 0$ occurring only as $\Delta t = 25ms$, thus supporting the abrupt nature of reset transition. In addition, even under the same operation mode, the experimental data exhibit a large variability due to the stochastic nature of RS, whose impact becomes more serious for increasing Δt. The distribution of variability is also calculated by Monte Carlo simulations and the result, similar to experimental one, is shown in Figure 6(b).

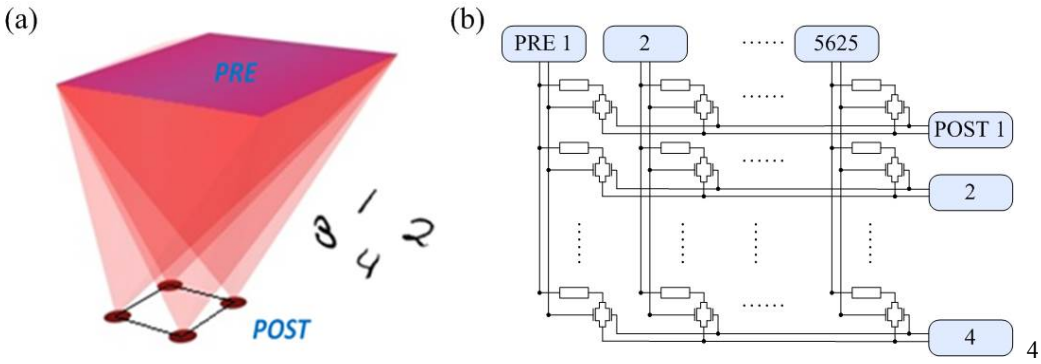

Figure 7. (a) Conceptual representation and (b) corresponding circuital scheme of a feedforward 2-layer neuromorphic network for multi-pattern learning. The network consists of a first layer with N=75x75 PREs and a second layer with M=4 POSTs, which are fully connected by perovskite-based 2T-1R synapses. To achieve multi-pattern learning, the 4 POSTs communicate via inhibitory synapses whose function is to hinder that more POSTs specialize on the same input pattern.

To demonstrate in simulation multi-pattern learning and recognition, we designed a 2-layer neuromorphic network consisting of a first layer with N = 75x75 PREs as and a second layer with $M = 4$ POSTs. Figure 7 (a) and (b) shows the schematic illustration and the circuit implementation of the simulated neuromorphic network. PRE and POST communicate via 2T1R synapses according to operation scheme

illustrated in Figure 5. The first layer acts as an artificial retina since emits spikes in correspondence of submission of a visual pattern. In addition to pattern (black) pixels, a submitted image also presents background (white) pixels, which are labeled as noise. Note that in our implementation, PREs are solely stimulated by black pixels corresponding to the submitted pattern.

As previously mentioned, each POST integrates the synaptic currents induced by all the active pixels and sends a fire spike as the internal potential reaches an internal firing-threshold.

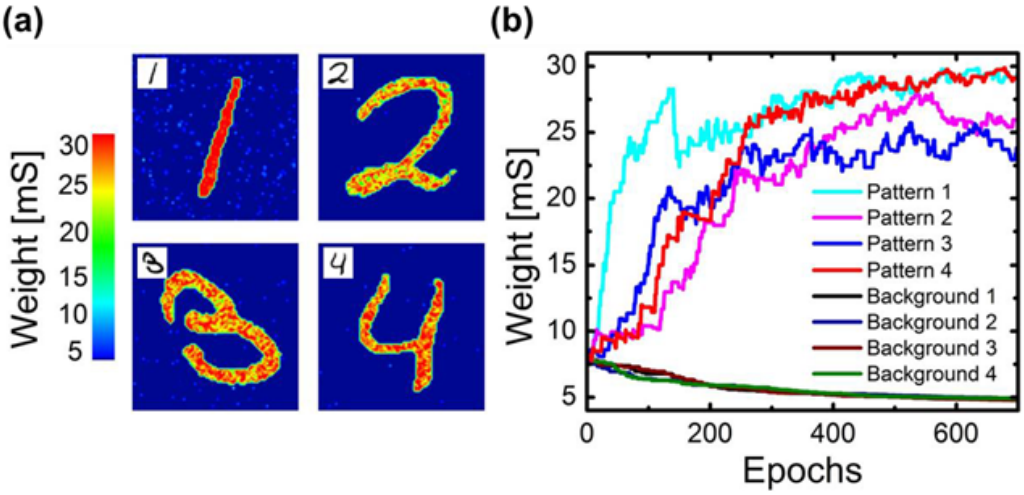

Figure 8. (a) Color maps of synaptic weights at the end of training phase revealing the parallel learning of 4 different visual patterns (shown in the top left insets) submitted to the neuromorphic network. (b) Evolution of mean synaptic weights for all the submitted patterns and their corresponding background for increasing epochs evidencing a gradual potentiation of pattern synapses and a faster depression of respective background synapses.

Figure 8(a) shows four specific visual patterns extracted from the MNIST dataset [29] representing the handwritten digits “1”, “2”, “3” and “4” to demonstrate the

capability of unsupervised multi-pattern learning and recognition by our RRAM-based neuromorphic network.

During learning phase, the input feeding the PRE-layer at any time can be either one of 4 handwritten digit patterns, each one with equal probability, or random noise. Particularly, the presentation probability of pattern and random noise is set to 50%.

At each epoch, we also set different amounts of plastic excitatory synapses, namely 650 for noise and 90 for pattern. All the synapses were prepared in a random resistance state. As result of training phase, which lasts 700 epochs, each of 4 input patterns has been successfully learnt in a single POST because of the inhibitory connections among them (Figure 8(a)), thus supporting unsupervised learning capability of our network. This result is also confirmed by Figure 8(b) where the evolution of mean synaptic weights is calculated as a function of the training epochs. It should be noted that on one side pattern synapses converge to LRS within 300 epochs via anti-LTD process while on the other side background synapses only need 200 epochs to achieve the HRS state via anti-LTP process, thus supporting again the nature of RS in perovskite-based RRAM described in Figure 6. Finally, the obtained evolution results sufficiently stable despite the fluctuations of mean weights of background and pattern synapses at every learning epoch.

Conclusion

In this work, we have proposed an analytical compact model for $CH_3NH_3PbI_3$ organic-inorganic perovskite-based RRAM to obtain an essential tool to design large-scale systems including RRAM devices for attractive applications such as

neuromorphic or logic computing.

Our model shows a nice agreement with experimental measurements and allows to explore in detail the evolution of physical parameters, such as local temperature, the radius and height of CF, governing RS in RRAM devices. Based on this model, we first achieve in simulation anti-STDP characteristics at level of single device, which are clearly consistent with curves obtained in experiments by taking also account of the inherent variability of these resistive devices. Finally, we simulated a 2-layer neuromorphic network with 2T1R synapses by demonstrating unsupervised learning and recognition of 4 visual patterns from MNIST handwritten digit database. Our results are very promising and pave the way for the use of perovskite-based RRAM devices in very large circuit systems capable of neuromorphic computation.

Acknowledgements

We thank Dr. Stefano Ambrogio for the helpful discussions on the pattern learning and recognition. This work was supported by the NSFC for Excellent Young Scholars (No. 51422201), the NSFC Program (Nos. 51732003, 51372035, 61774031, 61574031, 61404026, and 11604044), the "111" Project (No. B13013), the Fund from Jilin Province (No. 20160101324JC), and the European Research Council (ERC) under the European Union's Horizon 2020 research and innovation programme (grant agreement No. 648635).

Conflict of Interest

The authors declare no conflict of interest.

Keywords

analytical modeling, neuromorphic computing, organic–inorganic perovskites, resistive switching

Reference

[1] F. Pan, S. Gao, C. Chen, C. Song, and F. Zeng, "Recent progress in resistive random access memories: Materials, switching mechanisms, and performance," *Materials Science and Engineering: R: Reports*, vol. 83, pp. 1–59, Sep. 2014.

[2] H. Wu, X. Li, M. Wu, F. Huang, Z. Yu, and H. Qian, "Resistive Switching Performance Improvement of Ta_2O_{5-x}/TaO_y Bilayer ReRAM Devices by Inserting AlO_δ Barrier Layer," *IEEE Electron Device Letters*, vol. 35, no. 1, pp. 39–41, Jan. 2014.

[3] E. Piccinini *et al.*, "Hot-carrier trap-limited transport in switching chalcogenides," *Journal of Applied Physics*, vol. 112, no. 8, 2012.

[4] Z. Xiao and J. Huang, "Energy-Efficient Hybrid Perovskite Memristors and Synaptic Devices," *Advanced Electronic Materials*, vol. 2, no. 7, p. 1600100, Jul. 2016.

[5] X. Zhu, J. Lee, and W. D. Lu, "Iodine Vacancy Redistribution in Organic-Inorganic Halide Perovskite Films and Resistive Switching Effects," *Advanced Materials*, p. 1700527, Jun. 2017.

[6] J. X. Zhu *et al.*, "Flexible, transferable and conformal egg albumen based resistive switching memory devices," *RSC Adv.*, vol. 7, no. 51, pp. 32114–32119, 2017.

[7] D. Bi *et al.*, "Polymer-templated nucleation and crystal growth of perovskite films for solar cells with efficiency greater than 21%," *Nature Energy*, vol. 1, no. 10, p. 16142, Sep. 2016.

[8] X. Y. Chin, D. Cortecchia, J. Yin, A. Bruno, and C. Soci, "Lead iodide perovskite light-emitting field-effect transistor," *Nature Communications*, vol. 6, p. 7383, Jun. 2015.

[9] J. Luo *et al.*, "Water photolysis at 12.3% efficiency via perovskite photovoltaics and Earth-abundant catalysts," *Science*, vol. 345, no. 6204, pp. 1593–1596, Sep. 2014.

[10] J. Choi *et al.*, "Organolead Halide Perovskites for Low Operating Voltage Multilevel Resistive Switching," *Advanced Materials*, vol. 28, no. 31, pp. 6562–6567, Aug. 2016.

[11] C. Gu and J.-S. Lee, "Flexible Hybrid Organic–Inorganic Perovskite Memory," *ACS Nano*, vol. 10, no. 5, pp. 5413–5418, May 2016.

[12] S. Long, C. Cagli, D. Ielmini, M. Liu, and J. Suñé, "Analysis and modeling of resistive switching statistics," *Journal of Applied Physics*, vol. 111, no. 7, 2012.
[13] D. Ielmini, F. Nardi, and S. Balatti, "Evidence for voltage-driven set/reset processes in bipolar switching RRAM," *IEEE Transactions on Electron Devices*, vol. 59, no. 8, pp. 2049–2056, 2012.
[14] Z. Jiang *et al.*, "A Compact Model for Metal – Oxide Resistive Experiment Verification," *IEEE Transactions on Electron Devices*, vol. 63, no. 5, pp. 1884–1892, 2016.
[15] J. F. Kang *et al.*, "Modeling and design optimization of ReRAM," 2015, pp. 576–581.
[16] Z. Zhou *et al.*, "The Characteristics of Binary Spike-Time-Dependent Plasticity in HfO2-Based RRAM and Applications for Pattern Recognition," *Nanoscale Research Letters*, vol. 12, no. 1, Dec. 2017.
[17] P. Gu *et al.*, "Technological exploration of rram crossbar array for matrix-vector multiplication," *The 20th Asia and South Pacific Design Automation Conference*, pp. 106–111, 2015.
[18] P. Yao *et al.*, "Face classification using electronic synapses," *Nature Communications*, vol. 8, p. 15199, May 2017.
[19] D. Bhattacharjee, A. Siemon, E. Linn, and A. Chattopadhyay, "Efficient complementary resistive switch-based crossbar array Booth multiplier," *Microelectronics Journal*, vol. 64, pp. 78–85, Jun. 2017.
[20] S. Agarwal *et al.*, "Energy Scaling Advantages of Resistive Memory Crossbar Based Computation and Its Application to Sparse Coding," *Frontiers in Neuroscience*, vol. 9, Jan. 2016.
[21] P. M. Sheridan, F. Cai, C. Du, W. Ma, Z. Zhang, and W. D. Lu, "Sparse coding with memristor networks," *Nature Nanotechnology*, May 2017.
[22] S. Ambrogio, S. Balatti, D. C. Gilmer, and D. Ielmini, "Analytical modeling of oxide-based bipolar resistive memories and complementary resistive switches," *IEEE Trans. Electron Devices* **61**(7), pp. 2378-2386 (2014).
[23] J. M. Azpiroz, E. Mosconi, J. Bisquert, and F. De Angelis, "Defect migration in methylammonium lead iodide and its role in perovskite solar cell operation," *Energy Environ. Sci.*, vol. 8, no. 7, pp. 2118–2127, 2015.
[24] E. Mosconi, D. Meggiolaro, H. J. Snaith, S. D. Stranks, and F. De Angelis, "Light-induced annihilation of Frenkel defects in organo-lead halide perovskites," *Energy Environ. Sci.*, vol. 9, no. 10, pp. 3180–3187, 2016.
[25] D. W. deQuilettes *et al.*, "Photo-induced halide redistribution in organic–inorganic perovskite films," *Nature Communications*, vol. 7, p. 11683, May 2016.
[26] G.-Q. Bi and M.-M. Poo, "Synaptic modifications in cultured hippocampal neurons: dependence on spike timing, synaptic strength, and post synaptic cell type," *J. Neurosci.* **18**(24), pp. 10464–10472 (1998).
[27] L. F. Abbott and S. B. Nelson, "Synaptic plasticity: taming the beast," *Nat. Neurosci.* **3**(Suppl), pp. 1178–1183 (2000).
[28] Z. Wang, S. Ambrogio, S. Balatti, and D. Ielmini, "A 2-transistor/1-resistor artificial synapse capable of communication and stochastic learning in

neuromorphic systems," *Frontiers in Neuroscience*, vol. 8, Jan. 2015.
[29] Y. LeCun *et al.*, "Gradient-based learning applied to document recognition,", *Proc. IEEE* **86**(11), pp. 2278-2324 (1998).